Cell-specific inhibitory modulation of sound processing in the auditory thalamus.

Rolón-Martínez, S[1]., Mendoza, A.J.[2], Angeloni, C.F.[1], Chen, R.[1], Haas, J.S.[2], Geffen M.N.[1] *

[1]*Department of Otorhinolaryngology, University of Pennsylvania, Philadelphia, PA, United States*

[2]*Department of Biological Sciences, Lehigh University, Bethlehem, PA, United States*

*Corresponding author:
Maria Neimark Geffen, Ph.D. (she/her)
Department of Otorhinolaryngology
Perelman School of Medicine
University of Pennsylvania
5 Ravdin
3400 Spruce St.
Philadelphia PA 19104
Tel.: 215.898.0782

ABSTRACT

Inhibition along the auditory pathway is crucial for processing of acoustic information. Within the auditory thalamus, a key region in the central auditory pathway, inhibition is provided by the thalamic reticular nucleus (TRN), comprised of two large classes of inhibitory neurons, parvalbumin (PV^{TRN}) and somatostatin (SST^{TRN}) positive. In the auditory cortex, PV and SST neurons differentially shape auditory processing. We found that the ventral MGB, the thalamic region in the direct ascending auditory pathway, receives inputs predominantly from PV^{TRN} neurons, whereas SST^{TRN} neurons project to the dorso-medial regions of MGB. Consistently, inactivating PV^{TRN} neurons increased sound-evoked activity in over a third of neurons in the vMGB, with another large fraction of neurons being suppressed. By contrast, inactivating SST^{TRN} neuronal activity largely reduced tone-evoked activity in vMGB neurons. Cell type-specific computational models revealed candidate circuit mechanisms for generating the bi-directional effects of TRN inactivation on MGB sound responses. These differential inhibitory pathways within the auditory thalamus suggest a cell-specific role for thalamic inhibition in auditory computation and behavior.

INTRODUCTION

Sensory perception is driven by an interplay of excitatory and inhibitory processing pathways in the brain. Throughout these pathways, inhibitory neurons shape how sensory information is transmitted within and between brain regions[1]. Within the auditory system, excitatory synapses between the auditory cortex (AC) and the auditory thalamic nucleus, the medial geniculate body (MGB), play a key role in fine-tuning peripheral sensory information[2,3]. Critical to this process are the inhibitory inputs to the MGB from the thalamic reticular nucleus (TRN) – a thin sheet of inhibitory neurons that envelops the thalamus[4–7]. The two dominant sub-classes of inhibitory neurons within the TRN are parvalbumin- (PV) and somatostatin- (SST) positive neurons, which differentially project to and modulate somatosensory thalamic nuclei and are also critical for auditory processing within the AC[1,8–13]. Yet it remains unknown whether and how these two sub-classes of inhibitory neurons of the TRN anatomically project to and functionally modulate the excitatory neurons in the auditory thalamus. The goal of the present study was to test the hypothesis that PV and SST neurons of the TRN differentially modulate sound responses in MGB.

The TRN is the primary source of inhibition to the sensory thalamic nuclei. Through its inhibitory projections to excitatory relay neurons, it filters relevant sensory information important for perception[14–16] and can support optimal behavioral performance in sensory attentional tasks[17–19]. Anatomical projections of the caudo-ventral area of the TRN, considered the auditory TRN (audTRN), target and envelop MGB[20]. MGB is anatomically subdivided into three main subnuclei: the ventral division (vMGB), the medial division (mMGB), and the dorsal division (dMGB). At a circuit level, the TRN receives excitatory information through projections from the MGB as well as from corticothalamic inputs from L5 and L6 neurons and then sends inhibitory projections back to MGB[5,21–25]. This pathway is generally thought to amplify sensory information within the MGB.

PV and SST neurons are present in other regions in the auditory pathway, and have been shown to play differential but critical functions within the auditory cortex[8,11,12,26–31]. These studies show that 1) SST, but not PV, neurons contribute to stimulus-specific adaptation (SSA), a phenomenon in which neurons adapt selectively to a subset of inputs presented frequently[26,27,32–36], and 2) PV and SST neurons differentially modulate frequency-dependent responses of excitatory neurons[11,12,27]. Activating PV or SST neurons leads to a decrease in frequency selectivity and an overall increase in tone responsiveness of cortical excitatory neurons[8,10,11,13]. Within the TRN, PV and SST function has been studied in the somatosensory system. PV and SST neurons of the TRN target distinct somatosensory thalamic nuclei involved in divergent thalamocortical circuits[9,37]. PV and SST

neurons of somatosensory TRN also have differential bursting properties and differentially modulate somatosensory behavior[9]. While it is therefore plausible that PV^{TRN} and SST^{TRN} neurons differentially control sound processing in the MGB, this has no been previously tested directly.

In this study, our goal was to quantify the differential effects of PV^{TRN} and SST^{TRN} neurons on thalamic sound processing. We used viral transfection methods to drive a soma-targeted inhibitory opsin in the TRN to inactivate PV^{TRN} or SST^{TRN} neurons while recording neuronal activity from neurons in the MGB of awake passively listening head-fixed mice. To anatomically identify how PV^{TRN} and SST^{TRN} neurons project to the sub-nuclei of the MGB, we used viral tracing techniques to express an anterograde virus encoding a flexed fluorescent reporter in TRN of transgenic PV-Cre or SST-Cre mouse lines and traced projections to the MGB. We found that PV^{TRN} and SST^{TRN} neurons target distinct subregions of the MGB and differentially modulate neuronal activity, consistent with the differences in their projection patterns. To further investigate circuit mechanisms that may underlie the unexpected bidirectional modulation resulting from inactivation of SST^{TRN} and PV^{TRN} neurons, we examined changes in MGB activity in computational models with varied synaptic connectivity within TRN and from TRN to MGB. These simulations highlight several variations of possibly-underappreciated thalamic circuitry that can explain the experimental results, including disynaptic inhibition and underappreciated divergent inhibition. Combined, our results provide a framework for understanding the function of subcortical excitatory-inhibitory interactions throughout circuits in the sensory systems.

RESULTS

PV and SST neurons of the TRN project to MGB, targeting different subregions.

We first imaged the distribution PV^{TRN} and SST^{TRN} neuronal projections in MGB using viral neuroanatomical tracing methods. We injected anterograde adeno-associated viruses into the TRN of PV-Cre or SST-Cre mice and traced the axonal projections to the MGB (**Figure 1A & 1C**). We took advantage of the finding that calretinin is solely expressed in the higher-order MGB[38] to characterize the projection patterns of both neuronal subtypes within the MGB. We labeled cell bodies in dorso-medial MGB using calretinin anti-body. The anterograde virus labeled axons in MGB from PV^{TRN} or SST^{TRN} neurons. Whereas PV^{TRN} neurons targeted the central portion of vMGB, SST^{TRN} neurons avoided this region. PV^{TRN} projections were stronger in the central area of ventral MGB rather than peripheral and dorso-medial regions (**Figure 1B;** *$N = 14$ ROIs, $p \leq 0.001$, signed-*

rank test). By contrast, projections of TRN^{SST} targeted the dorsal and medial MGB (**Figure 1D;** *N = 8 ROIs, p = .023, signed-rank test*). Combined, these data demonstrate that PV^{TRN} and SST^{TRN} neurons exhibit differential projection patterns to the MGB.

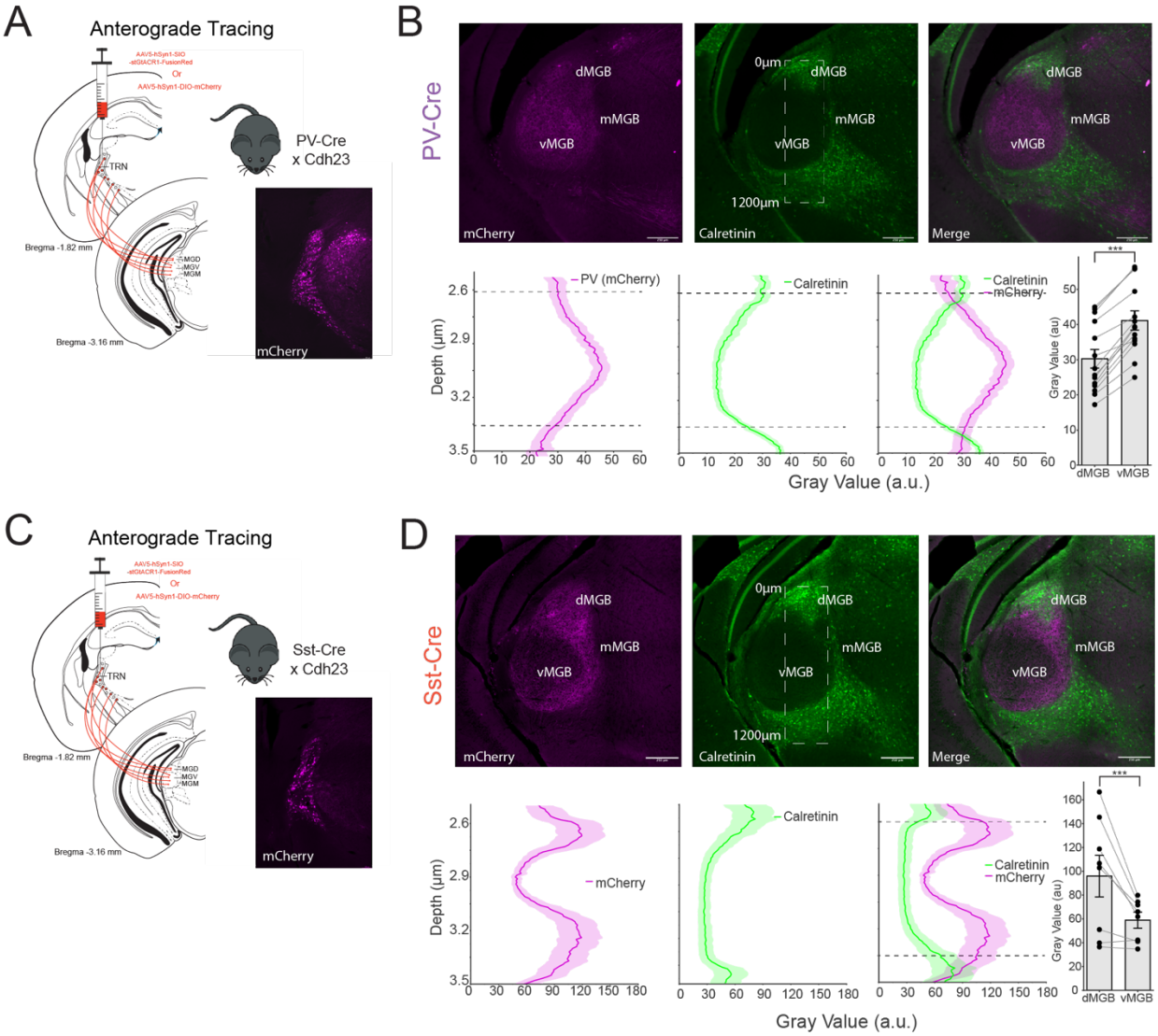

Figure 1. PV^{TRN} and SST^{TRN} project to different subregions of the MGB. A. Experimental design for anatomical experiments. PV-cre mice were injected with AAV5-hSyn1-DIO-mCherry into TRN for anterograde tracing of PV neurons in the TRN. Inset: mCherry expression in the TRN indicating the localization of the virus. **B. Top**: Projections of PV^{TRN} neurons primarily target the ventral subdivision of the MGB. *Left panel*: Viral expression of projections to the MGB (magenta). *Middle panel*: Immunohistochemical labeling of calretinin in the MGB (green). *Right panel*: Merged channels. **Bottom**: Quantification of the fluorescence intensity of projections from PV^{TRN} neurons that target MGB (Dashed box in top middle panel outlining the ROI). *Left panel*: intensity of viral expression of projections to the MGB in the ROI along the dorso-ventral axis. *Middle panel*: intensity of the immunohistochemical labeling of calretinin in the MGB in the ROI along the dorso-ventral axis. *Right panel*: merged channels. *Barplot:* mean intensity of the projections of PV-audTRN neurons in dorsal and ventral MGB (N =14 ROI's; n = 3). **C.** SST-cre mice were injected with AAV5-hSyn1-DIO-mCherry into TRN for anterograde tracing of SST neurons in the TRN. **B. Top**: Projections of SST^{TRN} neurons primarily target the ventral subdivision of the MGB. *Left panel*: Viral expression of projections to the MGB (magenta). *Middle panel*: Immunohistochemical labeling of calretinin in the MGB (green). *Right panel*: Merged channels. **Bottom**: Quantification of the fluorescence intensity of projections from SST^{TRN} neurons that target MGB (Dashed box in top middle panel outlining the ROI). *Left panel*: intensity of viral expression of projections to the MGB in the ROI along the dorso-ventral axis. *Middle panel*: intensity of the immunohistochemical labeling of calretinin in the MGB in the ROI along the dorso-ventral axis. *Right panel*: merged channels. *Barplot:* mean intensity of the projections of PV-audTRN neurons in dorsal and ventral MGB (N =8 ROIs; n = 3). *Scale bar = 0.25 mm. vMGB: ventral MGB; dMGB: dorsal MGB; mMGB: medial MGB; White dashed box in the top middle panel indicates ROI for fluorescence intensity quantification.*

Inactivation of PV^{TRN} and SST^{TRN} neurons differentially affects tone-evoked responses in the MGB.

Because of our anatomical results and previous work identifying genetically distinct TRN neurons that express different physiological properties[9,37], we next tested whether and how MGB neurons are modulated by PV^{TRN} and SST^{TRN} neurons. We inactivated SST and PV neurons in audTRN during tone-evoked responses in MGB neurons. We injected a Cre-dependent soma-targeted inhibitory opsin (AV5-hSyn-SIO-stGtACR1-FusionRed) in the audTRN of SST-Cre or PV-Cre mice. This virus only expresses in the soma of Cre-expressing neurons, reducing the chance of effects from backpropagating action potentials from local terminals[39]. We then implanted an optic fiber above audTRN, a headpost and a ground pin for awake *in-vivo* electrophysiological recordings. Mice passively listened to tones ranging from 3-80kHz, while we recorded and measured the spiking activity of MGB neurons. We quantified neuronal firing rate for both laser-off and laser-on conditions and calculated the difference between these conditions as a function of probe depth (**Figure 2A, 2B, 2F & 2G**).

We expected the PV^{TRN} neuronal inactivation would drive the disinhibition of responses of MGB neurons, which would be stronger in the central vMGB. By contrast, we expected that inactivating SST^{TRN} neurons would either not affect MGB activity, or would suppress MGB responses to sounds via a double inhibitory pathway. Because SST^{TRN} and PV^{TRN} are reciprocally connected, inactivating SSTs could disinhibit PVs which would in turn suppress MGB neurons. This effect would be stronger in the central regions of MGB, and there would be mixed effects in the dorsal regions of the MGB.

Indeed, inhibiting PV^{TRN} neurons facilitated sound-evoked responses in a large fraction of MGB neurons (**Figure 2C, 2D & 2E**). The facilitation was stronger for the medial regions of vMGB than dMGB (*$p = 0.0070$, binned by depth: 2.5-2.9mm versus 3.1-3.5 mm, rank-sum test*), and this change was exacerbated by the larger number of facilitates neurons in center vMGB (**Figure 2E**). Surprisingly, there was also a strong suppression of a fraction of neurons throughout vMGB. However, this suppression was not differential across MGB (*$p = 0.18$, rank-sum test)*. Inactivating SST^{TRN} neurons resulted in a dominant suppression of tone-evoked responses in MGB, with a handful of neurons exhibiting facilitation (**Figure 2H, 2I & 2J**). Furthermore, the suppression was stronger in the dorsal MGB as compared to vMGB (*$p = 0.000050$, rank-sum test*). These results demonstrate a differential mode of action for distinct inhibitory neuronal types in the TRN on thalamic neuronal activity.

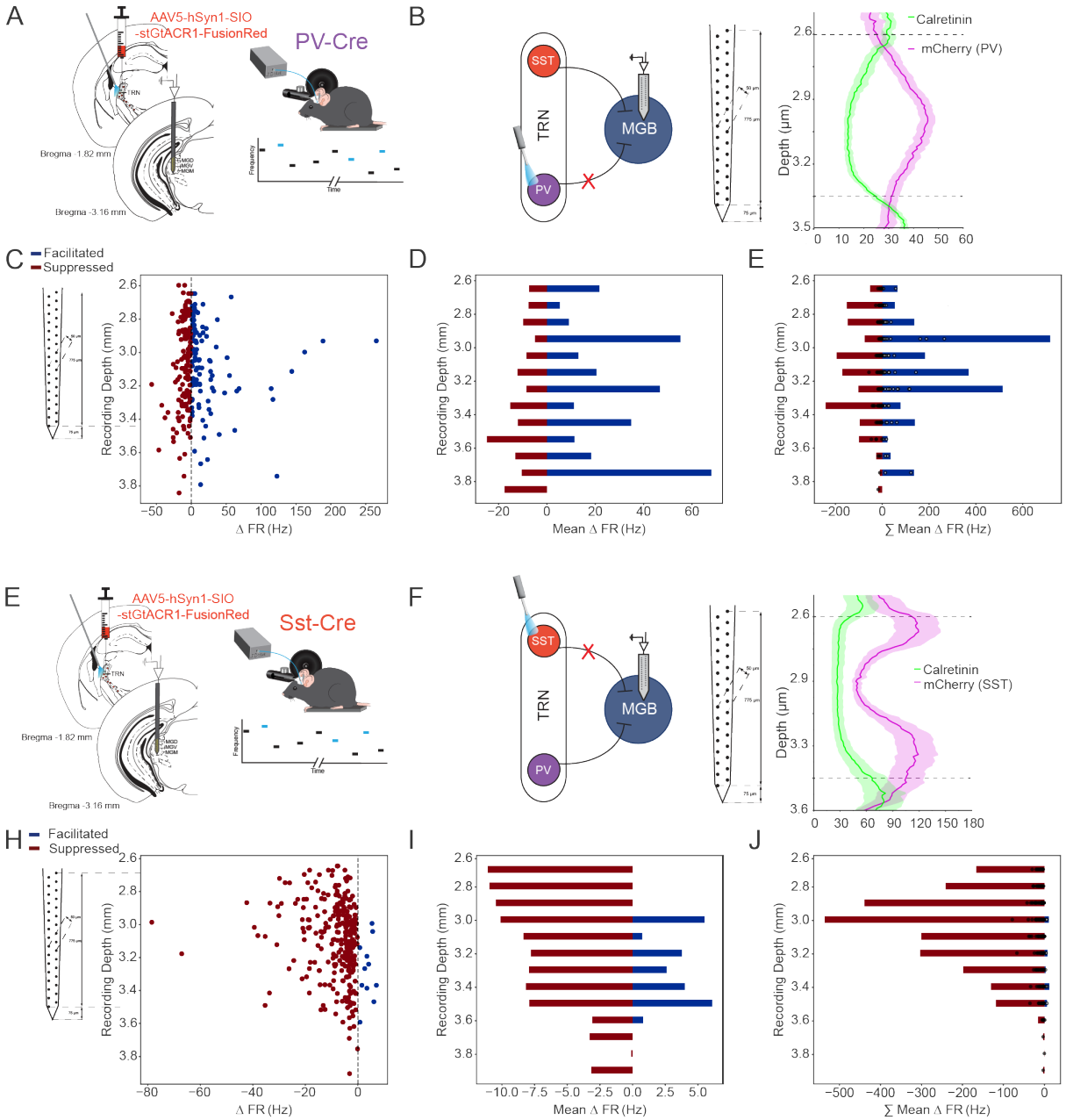

Figure 2. Inactivation of PV^{TRN} and SST^{TRN} neurons differentially affect tone-evoked activity in MGB neurons. A. PV mice were injected with a soma-targeted AAV5-hSyn1-DIO-stGtACR1-FusionRed into the audTRN and were implanted with an optic fiber. We recorded from MGB neurons in awake head-fixed mice. We presented a set of pure tones in light-on and light-off conditions. **B.** We selectively inactivated PV neurons of the audTRN while recording from neurons in the MGB using a vertical multi-channel electrode that spanned the depth of dMGB and vMGB, with the top electrode positioned at the tip of dMGB. **C.** Scatter plot showing the change in FR of recorded MGB neurons with PV^{TRN} inactivation as a function of probe depth. Red: suppressed neurons; Blue: facilitated neurons. **D.** Mean change in FR of recorded MGB neurons with PV^{TRN} inactivation as a function of probe depth in 100 µm bins. **E.** Total change in FR of recorded MGB neurons with PV^{TRN} inactivation as a function of probe depth in 100 µm bins. **F-J.** Same as **A-E**, but for SST^{TRN} inactivation. (N (PV) =239, n = 4. N (SST): 282, n = 4). ROIs; n = 3). *Scale bar = 0.25 mm. vMGB: ventral MGB; dMGB: dorsal MGB; mMGB: medial MGB; White dashed box in the top middle panel indicates ROI for fluorescence intensity quantification.*

Inactivation of PV^{TRN} neurons facilitates or suppresses tone-evoked responses in MGB.

We next examined in more detail the effect of inactivating PV^{TRN} neurons on tone-evoked responses in MGB. For a representative *facilitated* MGB neuron, the raster plots and post-stimulus time histograms (**Fig. 3A, B**) demonstrate an increase in activity during tone presentation. For this neuron, the increase was more pronounced at 0-25 ms after stimulus onset, and affected the responses across tone frequencies (**Fig. 3C**). The effects subsided in the 25-50 ms tone bin (**Fig. 3D**). For a representative *suppressed* MGB neuron, the raster plot and the PSTH depict reduction in spiking activity during the tone (**Fig. 3E, F**). The suppressive effects of SST^{TRN} inactivation were more pronounced at 0-25 ms (**Fig. 3G**), but persisted at 25-50 ms after tone onset (**Fig. 3H**).

Across the population of MGB neurons, during tone presentation, 35% of neurons were facilitated, 48% of neurons were suppressed and 17% of neurons in the MGB were not affected by PV^{TRN} inactivation (**Fig. 3I**). Average PSTH across facilitated neurons demonstrated a sharp peak followed by a prolonged decay in firing rate after tone onset (**Fig. 3J**). Similarly, for suppressed neurons, the effect of the laser in the absence of tone was prolonged, and with tone resulted in an overall decrease in peak tone-evoked response followed by a reduction in activity (**Fig. 3K**). Over the population, there was no significant effect of the laser during spontaneous activity prior to stimulus (**Fig. 3M**). Neuronal activity was significantly facilitated or suppressed both in the beginning (0-25 ms) and during the second half (25-50 ms) of the tone onset (**Fig. 3N, O;** *N (facilitated): 101, N = (suppressed): 138; p (facilitated-0-25ms) ≤ 0.001, p (suppressed-0-25ms) ≤ 0.001; p (facilitated-25-50ms) ≤ 0.001, p (suppressed-25-50ms) ≤ 0.001; signed-rank test*). When PV^{TRN} neurons were inactivated, time-to-peak significantly increased in the facilitated MGB neurons and decreased in the suppressed MGB neurons (**Fig. 3L;** *N (facilitated): 101, N = (suppressed): 138; p (facilitated-0-25ms) ≤ 0.001, p (suppressed-0-25ms) ≤ 0.017; signed-rank test*). This suggests that PVs selectively control time-to-peak in neuronal responses in MGB. Overall, these results demonstrate that the inactivating PV^{TRN} neurons rapidly affected tone-evoked responses in MGB, with effects persisting over the stimulus duration. PV^{TRN} neurons can both directly suppress neuronal responses in MGB, and, likely via reciprocal connections with SSTs and with each other, enhance the response firing rate.

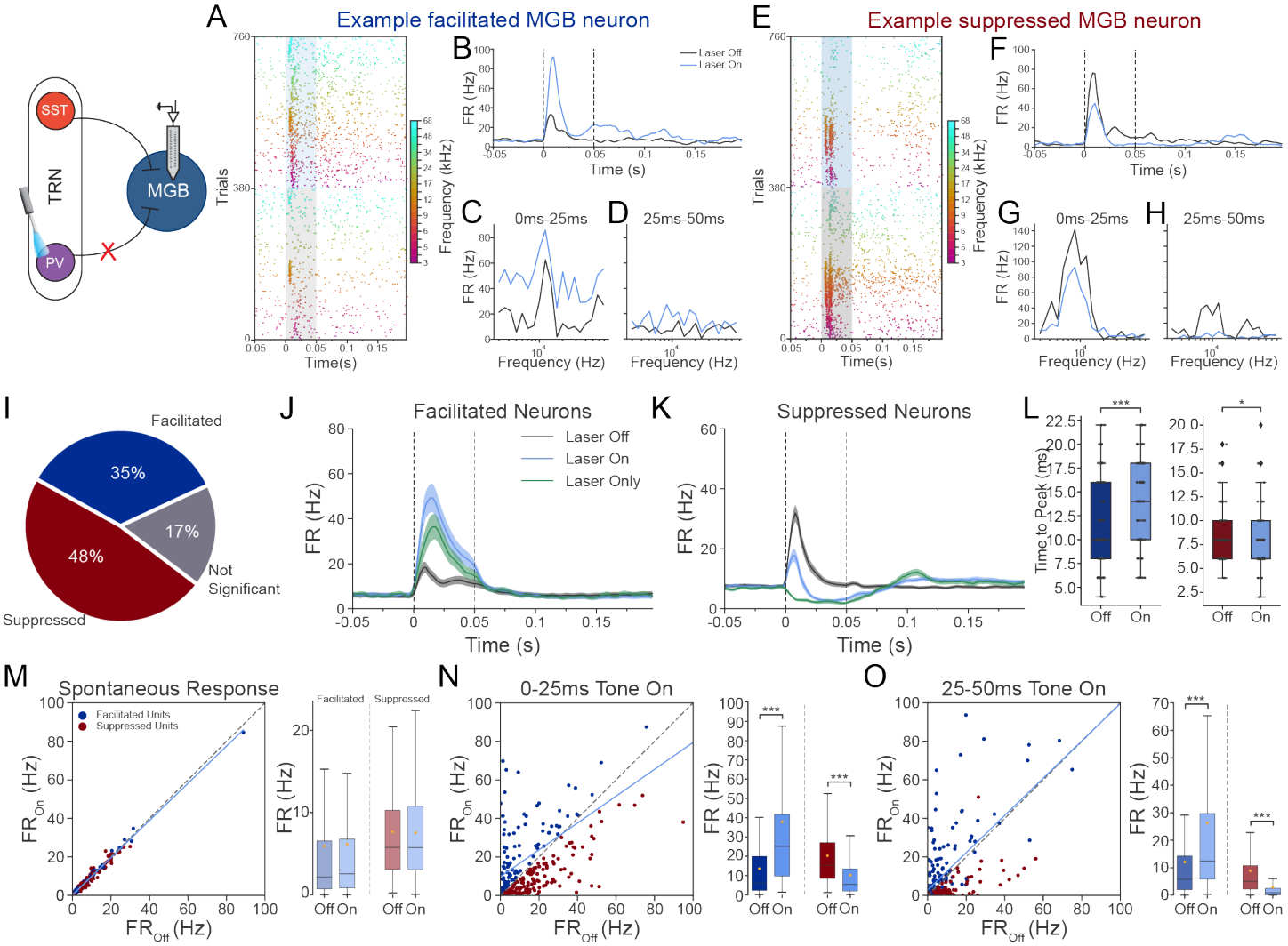

Figure 3. Inactivation of PV^{TRN} neurons facilitates and suppresses tone-evoked activity in MGB neurons. A. PV mice were injected with a soma-targeted AAV5-hSyn1-DIO-stGtACR1-FusionRed into the audTRN and were implanted with an optic fiber. We recorded from MGB neurons in awake head-fixed mice. We presented a set of pure tones in light-on and light-off conditions. We selectively inactivated PV^{TRN} neurons while recording from neurons in MGB. Raster plot of an example facilitated unit; trials are ordered by frequency and laser condition. The gray box indicates laser off conditions, blue box indicating the laser on conditions. **B.** PSTH of the facilitated example unit averaged across all trials for the laser off (black line) and laser on (blue line) conditions. **C.** Frequency response function for the facilitated unit during the first 25ms of tone presentation during laser off and laser on conditions. **D.** Frequency response function of the unit during the late 25-50ms of tone presentation. **E-H.** same as A-D, but for a representative facilitated neuron. **I.** Pie chart breaking down the effect of PV^{TRN} inactivation in neurons of the MGB. We find that 78% of recorded units had suppressed tone-evoked responses (red slice), 3% of recorded units had facilitated tone-evoked responses (navy blue slice), and 19% of tone-responsive units were not affected by laser manipulation (gray slice). **J,K.** Mean PSTH of facilitated (J) and suppressed (K) recorded neurons in MGB (N = 101 facilitated. N = 138 suppressed). Laser-only trials (green line), tone-only trials (black line), and tone- and laser-on trials (light blue line). **L.** Time to peak of tone-evoked responses for facilitated (left, blue) and suppressed (right, red) MGB neurons for laser offf (blue/red) and laser on (light blue) trials. **M-O.** Left: scatter plot, and right: box plot and boxplot of the mean FR for laser off and laser on conditions for facilitated (blue) and suppressed (red) neurons during spontaneous activity (**M**), 0-25 ms post stimulus onset (**N**), and 25-50 ms post stimulus onset (**)**). N = 239; n = 4. Shaded areas represent SEM±. Error bars represent SEM±. *** denotes p-value < 0.001; * denotes p-value < 0.05.

Inactivation of SST^{TRN} neurons primarily suppresses tone-evoked responses of MGB neurons.

We next examined in more detail the effect of inactivating SST^{TRN} neurons on tone-evoked responses of MGB neurons. For a representative facilitated MGB neuron, the rasterplots and post-stimulus time histograms (**Fig. 4A, B**) demonstrate an increase in activity at the onset of tone presentation. For this neuron, the increase was present at 0-25 ms after stimulus onset, and affected the responses selective to a region around the best frequency (**Fig. 4C**). The effects were not apparent in the 25-50 ms tone bin (**Fig. 4D**). For a representation suppressed MGB neuron, the raster plot and the PSTH depict reduction in spiking activity throughout the tone (**Fig. 4E, F**). The suppressive effects are more pronounced at 0-25 ms (**Fig. 4G**) but persist during the suppressed portion of tone response (**Fig. 4H**).

Across the population of neurons, during tone presentation, 78% neurons were suppressed, only 3% of neurons were facilitated and 19% of neurons in the MGB were not affected by SST^{TRN} inactivation (**Fig. 4I**). Average PSTH across the few facilitated neurons (N = 11 neurons) shows barely detectable amplification (**Fig. 4J**). For suppressed neurons, suppression driven by SST^{TRN} neuronal inactivation is prolonged in the absence of tone. In the presence of tone, the tone-evoked response is reduced and shortened (**Fig. 4K**). Over the population, there was no significant effect during spontaneous activity on laser-on versus laser-off trials prior to stimulus (**Fig. 4M**). Neuronal activity was significantly suppressed both in the beginning (0-25 ms) and during the second half (25-50 ms) of the tone onset (**Fig. 4N, O;** *N (facilitated): 11, N = (suppressed): 271; p (facilitated-0-25ms) = 0.001, p (suppressed-0-25ms) ≤ 0.001; p (facilitated-25-50ms) ≤ 0.147, p (suppressed-25-50ms) ≤ 0.001; signed-rank test*). although some cells, initially suppressed, exhibited facilitation in the second half of the tone. Unlike for PV^{TRN} suppression, there was no change in the time-to-peak response of MGB neurons upon inactivation of SST^{TRN} neurons (**Fig. 4L**). Overall, these results demonstrate that the inactivating SST^{TRN} neurons largely drove a suppression of MGB neurons. Remarkably, the time course of the effect of SST^{TRN} inactivation was very similar to that of PV^{TRN} inactivation for suppressed neurons. This suggests that potentially a similar network effect is engaged in driving MGB suppression with inactivation of either SST^{TRN} or PV^{TRN} neurons.

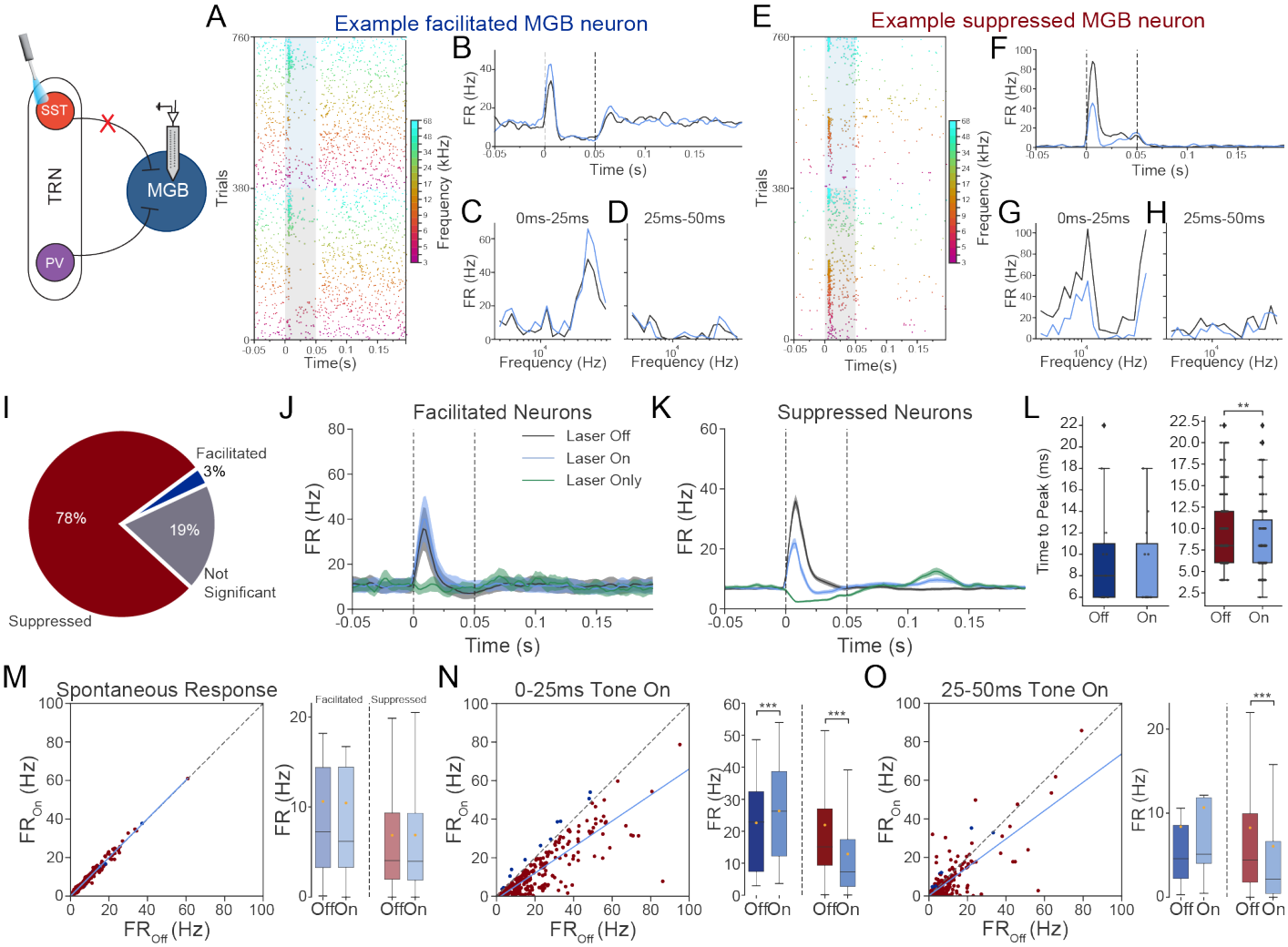

Figure 4. Inactivation of SST^{TRN} neurons facilitates and suppresses tone-evoked activity in MGB neurons. A. SST mice were injected with a soma-targeted AAV5-hSyn1-DIO-stGtACR1-FusionRed into the audTRN and were implanted with an optic fiber. We recorded from MGB neurons in awake head-fixed mice. We presented a set of pure tones in light-on and light-off conditions. We selectively inactivated SST^{TRN} neurons while recording from neurons in MGB. Raster plot of an example facilitated unit; trials are ordered by frequency and laser condition. The gray box indicates laser off conditions, blue box indicating the laser on conditions. **B.** PSTH of the facilitated example unit averaged across all trials for the laser off (black line) and laser on (blue line) conditions. **C.** Frequency response function for the facilitated unit during the first 25ms of tone presentation during laser off and laser on conditions. **D.** Frequency response function of the unit during the late 25-50ms of tone presentation. **E-H.** same as A-D, but for a representative facilitated neuron. **I.** Pie chart breaking down the effect of SST^{TRN} inactivation in neurons of the MGB. We find that 78% of recorded units had suppressed tone-evoked responses (red slice), 3% of recorded units had facilitated tone-evoked responses (navy blue slice), and 19% of tone-responsive units were not affected by laser manipulation (gray slice). **J,K.** Mean PSTH of facilitated (J) and suppressed (K) recorded neurons in MGB (N = 11 facilitated. N = 271 suppressed). Laser-only trials (green line), tone-only trials (black line), and tone- and laser-on trials (light blue line). **L.** Time to peak of tone-evoked responses for facilitated (left, blue) and suppressed (right, red) MGB neurons for laser offf (blue/red) and laser on (light blue) trials. **M-O.** Left: scatter plot, and right: box plot and boxplot of the mean FR for laser off and laser on conditions for facilitated (blue) and suppressed (red) neurons during spontaneous activity (**M**), 0-25 ms post stimulus onset (**N**), and 25-50 ms post stimulus onset (**O**). N = 282; n = 4. Shaded areas represent SEM±. Error bars represent SEM±. *** denotes p-value < 0.001; * denotes p-value < 0.05.

PV^{TRN} and SST^{TRN} differentially affect frequency tuning of MGB neurons.

Recordings in the auditory cortex (AC) find that inhibition of PV and SST interneurons produce changes in gain and tuning of excitatory pyramidal neurons of AC [11,12,27]. Given the lack of robust local inhibitory networks within the MGB [40], we hypothesized that PV^{TRN} and SST^{TRN} neurons differentially modulate gain and frequency tuning of neurons of the MGB.

Inactivation of PV^{TRN} neurons produced significant changes in MGB tuning for both the facilitated- and suppressed-tone evoked activity groups; with a significant shift upwards and a significant shift downwards in the frequency response function, respectively (**Figure 5A & Figure 5B;** *N (facilitated): 101, N = (suppressed): 138; p (facilitated-all octaves) ≤ 0.001, p (suppressed-all octaves) ≤ 0.001; signed-rank test*). Interestingly, in facilitated MGB neurons, response to best frequency decreased, but there was still a significant increase in the response to the sideband frequencies (**Figure 5A;** *N (facilitated): 101, N = (suppressed): 138; p (facilitated-sidebands) ≤ 0.001, p (facilitated-best frequency) = 0.204; signed-rank test*). Furthermore, we found that inactivation of PV^{TRN} significantly affected sparseness in both subgroups. Following of PV^{TRN} inactivation, facilitated MGB neurons significant decreased the sparseness index, becoming more broadly tuned (**Figure 5A;** *N (facilitated): 101; p (both time points) ≤ 0.001; signed-rank test*). The suppressed MGB neurons significantly increased the sparseness index, making becoming more narrowly tuned (**Figure 5B;** *N (suppressed): 138; p (both time points) ≤ 0.001; signed-rank test*). These results indicate that of PV^{TRN} neurons contribute to how narrowly or broadly tuned MGB neurons are to auditory stimuli in an output-dependent manner.

Inhibition of SST^{TRN} neurons produced no significant changes in tuning for MGB neurons that have facilitated tone-evoked responses (**Figure 5C;** *N (facilitated): 11; p (0-25ms) ≥ 0.05; signed-rank test*). However, MGB neurons that had suppressed tone-evoked firing rates show a significant downward shift in the frequency response function during the first 25ms of the tone presentation and the remaining 25ms of tone presentation (**Figure 5B;** *N = (suppressed): 271; p (both time points) ≤ 0.05; signed-rank test*). To examine frequency selectivity of neurons– or how specific neuronal responses are to a particular stimulus–we calculated the sparseness index. A value closer to 1 indicates that the unit responds narrowly to a set of stimuli and a value closer to 0 indicates that units will respond to a broader range of stimuli. We found that inactivation of SST^{TRN} neurons did not affect sparseness in the facilitated group (**Figure 5C***; N (facilitated): 11; p (0-25ms) = 0.638*; *p (25-50ms) = 0.765*; *signed-rank test*) however, the sparseness index in the suppressed group of neurons was

significantly increased (**Figure 5D;** *N (suppressed): 101; p (both time points) ≤ 0.001; signed-rank test*). Together, these results indicate that SST neurons of the TRN contribute to how narrowly or broadly tuned MGB neurons are to auditory stimuli.

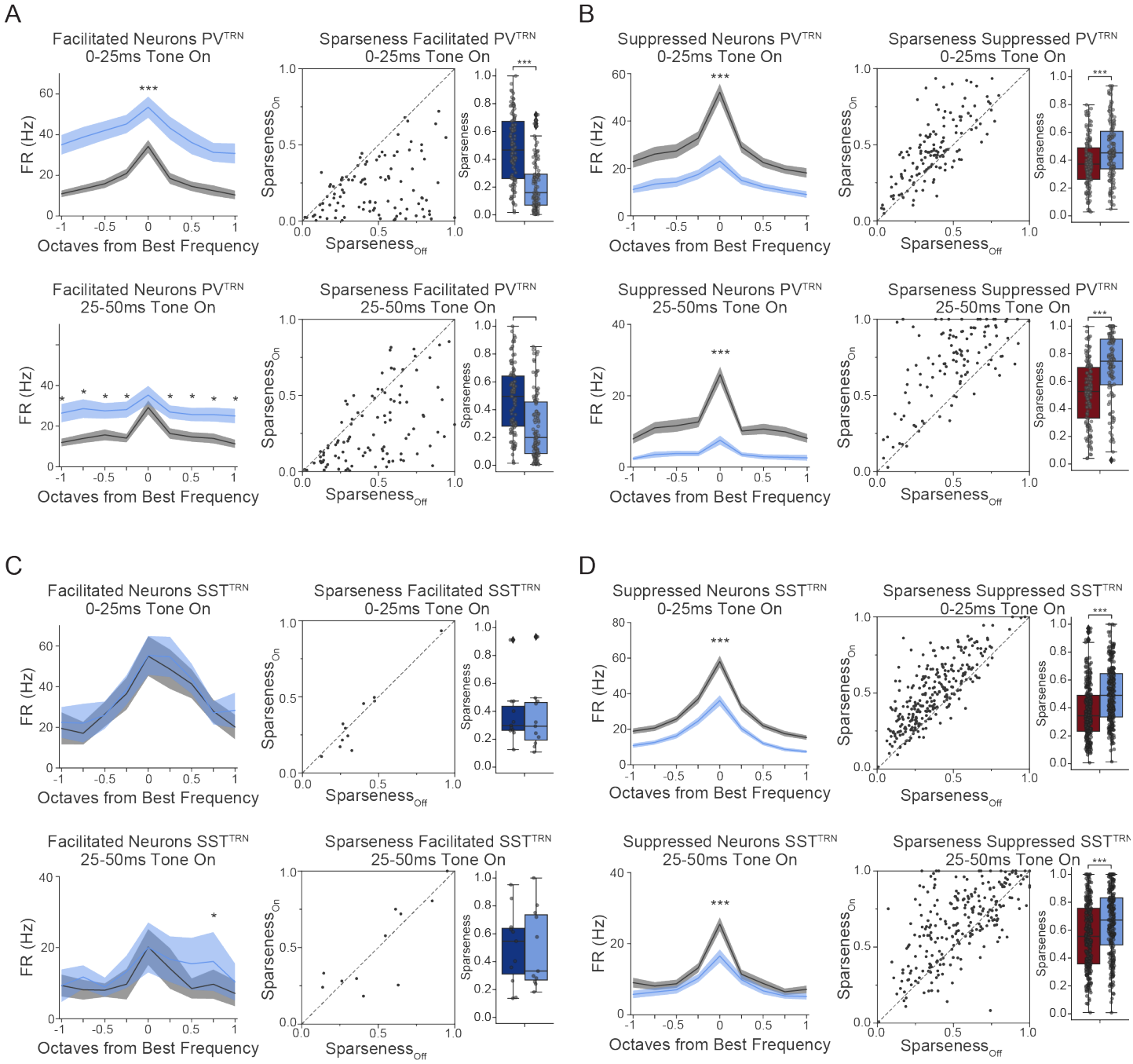

Figure 5. Inactivation of SST^TRN and PV^TRNneurons differentially affect frequency tuning of MGB neurons. A. Inactivation of audTRN-SST neurons. A. Diagram of experiment (PV^TRN inactivation, A; SST^TRN inactivation, G). **B-E.** *Left:* Mean frequency response function for laser on (light blue) and laser off (light gray) trials for neurons centered on best frequency (0 octaves = BF). Shaded areas represent SEM±. *Right*. Scatterplot of sparseness. **B, C.** Facilitated neurons. **D, E.** Suppressed neurons. **B, D.** 0-25 ms post stimulus onset. **C, E.** 25-50 ms post stimulus onset. **F-J.** Same as A-E, but for suppressed neurons. N = 239; n = 4 (PV). N = 282; n =4 (SST) Shaded areas represent SEM±. Error bars represent SEM±. *** denotes p-value < 0.001; * denotes p-value < 0.05.

Specifics of connectivity between MGB-TRN circuits determine the sign of MGB responses during TRN cell-type inactivation.

To examine the many possible connectivity schemes within TRN of primary and higher-order auditory thalamocortical circuits that may account for the observed changes in sensory responses during inactivation of specific TRN populations, we constructed a 4-cell model containing a primary vMGB relay cell reciprocally connected to a PV^{TRN} cell, in addition to a higher-order MGB cell reciprocally connected to a SST^{TRN} cell (**Figure 6A**), matching the subtype-specific connections that we identified and have been previously demonstrated for other sensory modalities[9,37]. TRN and MGB cells were single-compartment Hodgkin-Huxley models that include T currents. To match the reduced bursting properties in SST^{TRN} and higher-order MGB cells[9,41], those cells had 50% reduced T current densities (0.375 mS/cm^2). Tone inputs were simulated as exponentially decaying current pulses (peak amplitude 2.7 μA/cm^2, with decay time constant 30 ms) delivered simultaneously to each of the MGB cells. Each of the TRN cells was inactivated individually through a static conductance of 10 mS/cm^2 and reversal potential of -70 mV for 100 ms during the inputs (**Figure 6B**). Chemical synaptic connections between TRN cells were set at 1 μA/cm^2 for excitatory synapses from MGB to TRN cells, and 3 μA/cm^2 for all inhibitory synapses originating from TRN. For each stimulus condition, we repeated 150 trials under Poisson random noise of 0.2 μA at a rate of 80 Hz for excitatory and 20 Hz for inhibitory events. Among these trials, we varied the percent of trials that included various synaptic connections from TRN cells (**Figure 6C**). Subthreshold current steps of 0.3 μA were applied to all cells to increase excitability.

We first examined the effect of PV^{TRN} and SST^{TRN} inactivation on the responses of the primary vMGB cell to sensory input in circuits with differing connectivity between the TRN cells (**Figure 6D-F**). Without connectivity between columns, inactivation of the PV^{TRN} cell always allowed substantially increased responses in the vMGB firing rate to a tone input, whereas inhibiting the SST^{TRN} cell has no effect at all on vMGB response, as expected (not shown). Those trials served as a control for subsequent trials. Electrical synapses extensively couple TRN cells, including coupling between subtypes[42], that may substantially modulate activity within the thalamocortical circuits examined here[43,44]. We examined the effect of inter-type TRN coupling, using an electrical synapse with coupling coefficient ~0.2, on the responses of the primary MGB cell; similar to the uncoupled control case, vMGB responses were facilitated when PV^{TRN} was inactivated (**Figure 6D**, left). Similar to the unconnected circuit, we saw no changes in vMGB responses with the inclusion of an electrical synapse between PV^{TRN} and SST^{TRN} cells during inactivation of SST^{TRN} (**Figure 6D, right**). Although the existence of

inhibitory synapses between TRN neurons in mature tissue has been controversial [45], there is some evidence for lateral inhibition within TRN[46,47]. Inclusion of a lateral inhibitory synapse from SST^{TRN} to PV^{TRN} allowed a facilitated vMGB response during PV^{TRN} inactivation, and we noted that MGB responses during no-inactivation trials were also elevated from the control response (**Figure 6E, left**). Silencing SST^{TRN} cells in this circuit produced a substantial reduction in the tone response of the vMGB neuron compared to control responses (**Figure 6E, right**), matching the experimental results (**Figure 2, 4**) through relief of disynaptic inhibition. Silencing either cell type in a circuit that included inhibitory connections from PV^{TRN} to SST^{TRN} did not reduce tone responses of vMGB, however (not shown). Thus, one specific form of intra-TRN connectivity, from SST^{TRN} to PV^{TRN} cells, is a candidate circuit mechanism underlying the unexpected suppression of MGB during cell type-specific TRN inactivation.

The circuit models above examined firing rate changes in MGB in simplified all-or-none connectivity scenarios. However, we anticipate that in real tissue, mixes of connectivity and strength will co-exist within a spectrum across these various schemes, which could also result in the unexpected observed MGB responses. To test the effect of heterogeneous circuitry on firing rate changes in primary vMGB cells, we varied the ratio of lateralization within the circuits over a set of trials. In circuits where TRN and MGB are reciprocally connected, varied amounts of lateral intra-TRN inhibition always produce facilitation of vMGB responses when PV^{TRN} is inactivated (**Figure 6F, left**); the effect of SST^{TRN} lateralization was only to modulate the total facilitation produced. During SST^{TRN} inactivation, increases in SST^{TRN} lateral inhibition suppressed MGB responses independently of the presence of PV^{TRN} lateral inhibitory synapses (**Figure 6F, top right**). We note that the addition of coupling between TRN cells allowed for bidirectionality in changes in vMGB rate when SST^{TRN} was inactivated, for networks with weak SST-to-PV lateralization (**Figure 6F, bottom right**). From this set of simulations addressing intra-TRN connectivity, we conclude that inactivating SST^{TRN} can reproduce the unexpected suppression of vMGB response when SST-to-PV synapses or gap junctions are included (**Figure 4**); however, lateral intra-TRN connections alone cannot reproduce the bidirectional effects of PV^{TRN} inactivation (**Figure 3**). Next, we asked how the responses of primary vMGB might change during cell type-specific inactivation in the context of variations in feedback inhibition. TRN cells send divergent inhibitory connections to several MGB cells but often do not send inhibition back to the same cell that excite them[48,49]. Additionally, activation of one thalamic nucleus can produce inhibition in nearby sensory-related nuclei (i.e. activation of POM evoking IPSCs at VPM) thought to arise from TRN[50,51]. Thus, we included and varied the amount of divergent

feedback inhibition from TRN to MGB in our circuits. When inactivating PV^{TRN} cells, inclusion of both reciprocal and divergent inhibitory feedback still produced facilitation of the vMGB response (**Figure 6G, left**). For inactivation of SST^{TRN} cells in the context of divergent inhibition, vMGB responses were facilitated when circuits contained both reciprocal and divergent inhibitory synapses (**Figure 6G, right**). In circuits with only divergent but lacking reciprocal inhibitory feedback, PV^{TRN} inactivation produced a suppression of vMGB response (**Figure 6H, left**). Thus, inclusion of divergent feedback is a candidate circuit for reproducing the experimental results of PV^{TRN} inactivation. In circuits with only divergent inhibitory feedback from TRN to MGB cells, SST^{TRN} inactivation produced greater facilitation of vMGB responses (**Figure 6H, right**). Thus, we conclude that uniformly divergent feedback inhibition is unlikely to account for the experimental observations of vMGB suppression during SST^{TRN} inactivation.

Finally, we asked if variations in the relative power of the two types of feedback inhibition, combined, could allow both vMGB enhancement and suppression during cell type-specific inactivation trials. Increasing the relative strength of the divergent inhibitory synapses decreased the responses of the vMGB cell, while increasing the strength of reciprocal inhibition increased those responses, during PV^{TRN} inactivation trials compared to the baseline firing rate (**Figure 6I, top left**). This is consistent with the bidirectionality of the experimental results for PV^{TRN} inactivation (**Figure 3**). SST^{TRN} inactivation produced only increases in vMGB activity, as divergent inhibitory ratio increased from zero (**Figure 6I, top left**), inconsistent with experiments. However, electrical coupling added to this circuitry allowed SST^{TRN} inactivation to diminish vMGB responses for weakly lateralized networks (**Figure 6I, middle**). Including SST^{TRN}-to-PV^{TRN} lateral inhibition in this case modulated the SST^{TRN} inactivation response towards more suppressed outcomes (**Figure 6I, bottom right).** Together, our simulations lead us to conclude that several possible combinations of reciprocal and divergent connections, together with electrical synapses or SST^{TRN}-to-PV^{TRN} inhibition, may be embedded within the thalamus and serve as the sources of the bidirectional vMGB responses observed during PV^{TRN} inactivation and the suppression during SST^{TRN} inactivation.

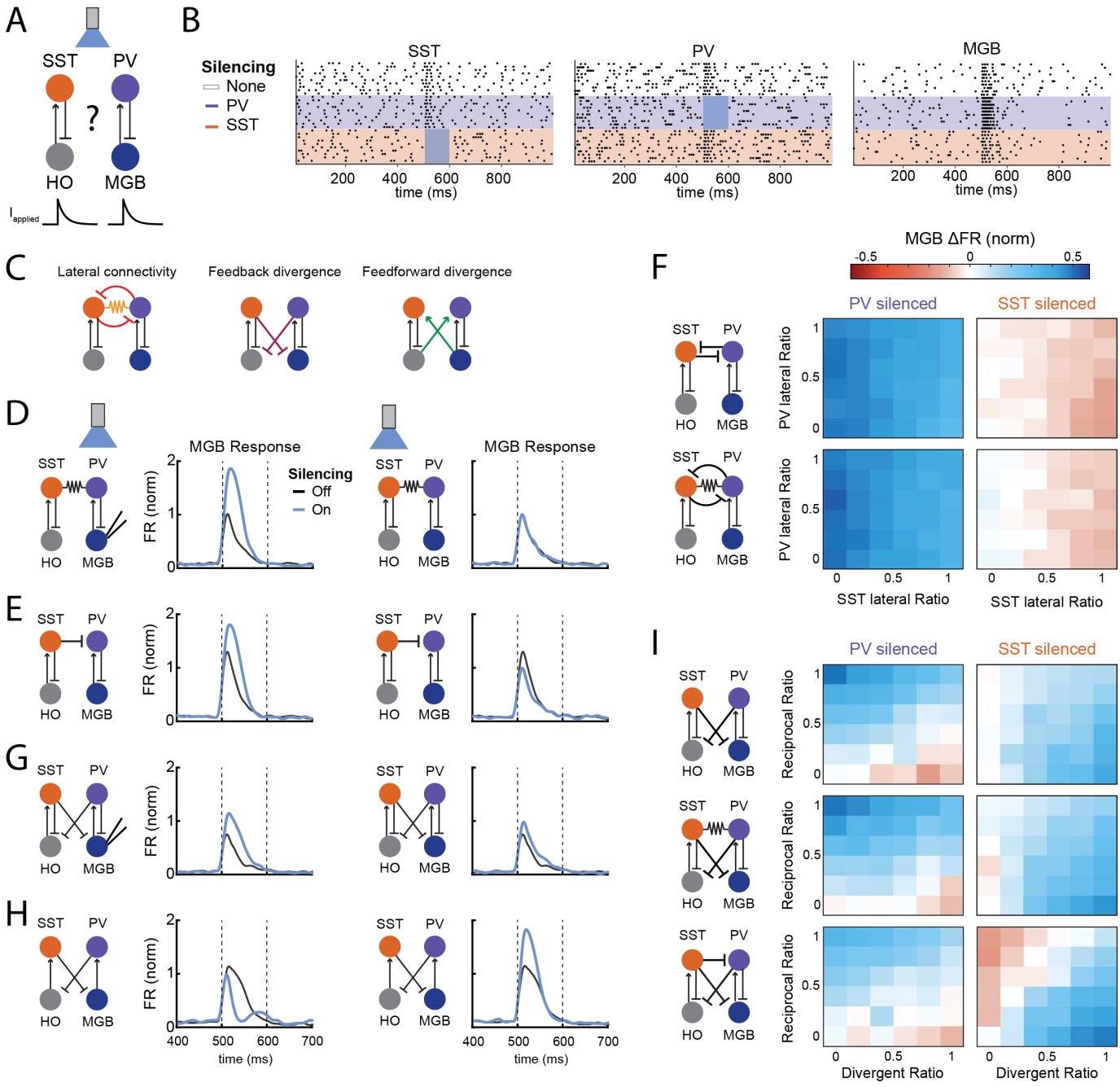

Figure 6. Schemes of circuit connectivity that account for bidirectional modulation of vMGB responses during subtype-specific inactivation in TRN. A. 4-cell model of primary sensory MGB-TRN pairs and higher order (HO) MGB-TRN pairs. **B.** Raster plots from trials with no inactivation, during PV inactivation (purple) and during SST^{TRN} inactivation (orange). **C.** Candidate connectivity schemes tested in models. **D.** PSTH of MGB firing for circuits with electrical coupling between TRN subtypes. MGB responses are normalized to the peak response during non-inactivated trials for no connectivity between columns. Left, primary MGB firing rate to input alone (black line) and with PV^{TRN} silencing (light blue line). Right, MGB firing rate input alone (black line) and with SST^{TRN} silencing (light blue line). **E.** As in D, for a circuit including lateral SST^{TRN} to PV^{TRN} connections. **F.** Effect of inactivation on MGB rate for heterogeneous combinations of lateral inhibitory connections, with and without electrical synapses between TRN cells. The ratio of lateral synapses is the percent of trials that included lateral synapses for each TRN cell type. **G.** As in D, for circuits with both reciprocal and divergent feedback inhibition. **H.** As in D, for circuits containing only divergent inhibition. **I.** Effect of cell type-specific inactivation on MGB rate for heterogeneous inhibitory feedback connections between TRN and thalamic cells. Divergence ratio is the percent of trials that included divergent synapses. Reciprocal ratio is the percent of trials that included reciprocal TRN-MGB synapses. Middle, with electrical coupling between PV and SST cells. Bottom, effect of inactivation on MGB rate with heterogeneous inhibitory connections in addition to lateral inhibition from the SST^{TRN} to PV^{TRN} cells.

DISCUSSION

The TRN is the main source of inhibitory information to all sensory thalamic structures[6,48,52]. The TRN– though entirely GABAergic[6] –is not homogenous in its molecular or genetic composition; neurons within the TRN exhibit a variety of genetic profiles, physiological properties, and distinct anatomical distributions[7,9,37,53] with PV and SST positive interneurons forming two major inhibitory classes. Furthermore, this differential anatomical distribution of TRN neurons is not limited to their topographical locations within the TRN, it also extends to how they project to their anatomical targets. Whereas the function of the TRN in the visual and somatosensory stimulus processing has been well described, less is known about how different neuronal subtypes of the auditory TRN shape how information is processing the auditory thalamus.

Here, we find that PV and SST neurons exhibit differential projection patterns in the MGB, with PV neurons primarily projecting to the center of the primary or first-order auditory thalamic sub-region (ventral MGB) and SST neurons avoiding the central region of vMGB, and projecting to the dorsal subregions of vMGB and higher-order auditory thalamic sub-regions (dorsal & medial MGB) (**Figure 1**). Inactivating these distinct subpopulations of audTRN inhibitory neurons had diverging effects on auditory tone responses of MGB neurons **(Figure 2)**. We expected that removing inhibition would facilitate MGB sound responses corresponding to their projection patterns. Indeed, we found that the inactivation of PV^{TRN} neurons facilitated a large fraction of MGB neurons whereas the inactivation of SST neurons barely drove any facilitated responses (**Figures 2, 3, 4**). By contrast, both manipulations resulted in a large fraction of neurons being disinhibited; this fraction was greater for SST neuronal inactivation.

Due to these varying internal physiological effects, we asked whether these different cell types have differential effects on tuning in the MGB. Given that PV and SST neurons differentially affect the tuning of excitatory cortical neurons within the auditory cortex[11,12,27], we hypothesized that distinct neuron types of the audTRN would drive differential physiological effects on auditory thalamic sound tuning. Our results show that inactivation of both PV^{TRN} and SST^{TRN} neurons resulted in changes in how narrowly or broadly tuned MGB neurons are **(Figure 5)**. These effects in the frequency response functions of the MGB relay neurons suggest that PV and SST neurons of the audTRN are critical for shaping auditory information at the level of the thalamus, as well as that in the auditory cortex.

Together, our anatomical, electrophysiological and simulation results indicate a nuanced role of TRN function on MGB neurons expanding their function beyond that of a direct inhibitory projection. A variety of

connection schemes have been proposed for TRN, including intra-TRN inhibition[46,46], lack of intra-TRN inhibition[45], typed reciprocal inhibition[9,37], and open-loop or divergent connectivity to thalamic nuclei[50,51]. In addition, gap junctions of the TRN could be exclusive within one set or both sets of cell types, or promiscuous across types[42], or absent in adult tissue. In order to better define the origin of the diverging effects of the PV and SST neuronal inactivation, we applied a computational model **(Figure 6)**. Our computational survey of these possibilities indicates that divergence of TRN-MGB connectivity is necessary, in addition to reciprocal inhibition, to achieve the bidirectional responses in MGB observed for PV inactivation; and that some intra-TRN connectivity, whether gap junctional or GABAergic, plays a role in allowing for the suppressive effects of SST inactivation. Detailed future experiments will be required to confirm and distinguish between these underappreciated possibilities.

We used a combination of viral anatomical tracing, optogenetics and awake *in-vivo* electrophysiological recordings to study the functional role of inhibitory neurons of the audTRN in modulating sound responses in the MGB. Viral tracing and optogenetic techniques allow us to express and manipulate specific types of neurons with the use of transgenic animals. Our data suggests that the differential output pattern of PV and SST neurons of the TRN to hierarchically distinct sensory thalamic regions is conserved across sensory modalities and may provide insights on the complexity of the audTRN. *In-vivo* awake recordings provide the ability to record neurons in an alert state and with little to no circuit disruption. However, our data analysis does not account for the feedback provided to MGB and TRN from the cortex. Within the auditory thalamus, the TRN provides most of the inhibitory information to MGB, however, the MGB also receives feedback from corticothalamic neurons in L5/L6 of AC as well as input from other association areas such as the BLA[23,54,55]. It is possible that the suppressive effects we observe when we disinhibit MGB from a specific cell type of the TRN, includes a component from fast feedback inhibition from another region of the brain. Future studies using high-density channel probes to record from multiple brain areas simultaneously can further our understanding of inhibitory circuit mechanisms. For example, recording from the TRN-MGB-AC circuit simultaneously while optogenetically manipulating 1) corticothalamic feedback, 2) TRN-MGB inhibitory synapses, or 3) collateral inputs from MGB to the TRN would allow recording effects of audTRN on neural responses along the auditory pathway.

One proposed mechanism for our results is the possibility of intra-TRN synapses between PV and SST neurons, similar to the interactions in cortical regions[1]. There have not been any GABAergic synapses found in the adult rodent TRN in slice preparations[45]. However, reports of dendro-dendritic synapses have been reported

in the TRN of the cat[56]. It has also been reported that excitatory collateral inputs from thalamic relay nuclei drive excitatory input onto TRN neurons and therefore activate TRN neurons[57]. It is possible that the suppression effects in tone-responsive units of the MGB is a direct result of fast feedback arising from excitatory MGB collaterals, intra-TRN dendro-dendritic synapses, or other regions of GABAergic inputs to the TRN like the basal forebrain, substantia nigra or lateral hypothalamus[58–61]. An extensive anatomical tracing study would specifically identify possible sources of GABAergic input to PV and SST neurons involved in the auditory pathway. This can reveal possible sources of feedback inhibitory inputs to the TRN that might drive the tone-evoked suppression we observe in our study.

TRN is a complex structure with cell types that vary in intrinsic physiological properties. PV and SST neurons of the somatosensory TRN have differential physiological properties, with PV neurons ehibiting higher levels of bursting than SST neurons[9]. Concurrent findings in TRN edge-zone and core-zone neurons and the genetically distinct *Spp1*$^{+}$ and *Ecel1*$^{+}$, show that core-zone and *Spp1*$^{+}$ which both receive input from FO thalamus are more likely to fire rebound bursts following hyperpolarization. However, edge-zone and *Ecel1*$^{+}$ fail to produce or have very few rebound bursts[37,53]. This can lead to speculation on how optogenetic manipulation during different stages of firing of TRN neurons can affect the synaptic properties. It would be of interest to study circuit mechanisms while recording the states of the TRN neurons while optogenetically manipulating the circuit. It would give greater insight into the importance of cellular mechanisms in inhibitory circuits.

The TRN and MGB are both highly functional brain regions involved in many behaviors. Recent studies have shown the contributions of HO-MGB to associative behavior memory tasks[62]. Our results show an specialized anatomical projection pattern of PV and SST neurons of the audTRN to the MGB with PV neurons primarily targeting ventral FO-MGB and SST neurons primarily targeting dorsal and medial HO-MGB. Whether and how disruption of inhibitory cell types of the TRN affects behavioral outputs of the MGB has yet to be explored. PV^{TRN} and SST^{TRN} neurons may play distinct roles in behaviors that rely on lemniscal versus non-lemniscal thalamic function.

Our results provide an insight into the complexity of the TRN and its function in sensory processing and identify cell-type specific mechanisms for controlling sound processing in the auditory thalamus.

MATERIALS AND METHODS

Animals.

We performed all experimental procedures in accordance with NIH guidelines on use and care of laboratory animals and by approval of the Institutional Animal Care and Use Committee at the University of Pennsylvania (protocol number 803266). Care was taken to minimize any pain, discomfort, or distress of the animals during and following experiments. Experiments were performed in adult male (n = 12) and female (n = 12) mice aged 3-8 months and weighing 20-32g. The mouse lines used in this study were crosses between Cdh23 mice (B6.CAST-Cdh23^{Ahl+}/Kjn; RRID:IMSR_JAX:002756)—a transgenic line that has a targeted point reversion in the Cdh23 gene which protects mice from age-related hearing loss [63]—and PV-Cre mice (B6.129P2-Pvalb$^{tm1(cre)Arbr}$/J; RRID:IMSR_JAX:017320) or SST-Cre mice (SST$^{tm2.1(cre)Zjh}$/J; RRID:IMSR_JAX:013044). Mice were housed at 28°C on a reversed 12hr light-dark cycle with ad libitum access to food and water. Experiments were performed during the animals' dark cycle and housed individually in an enriched environment after major surgery. Euthanasia was performed by infusion of a ketamine (300mg/kg) and dexmedetomidine (3mg/kg) cocktail or prolonged exposure to CO2. Both methods are consistent with the recommendations of the American Veterinary Medical Association (AVMA) Guidelines on Euthanasia.

Surgical Procedures.

Mice were induced to a surgical plane of anesthesia with 3% isoflurane in oxygen and secured in a stereotaxic frame. Animals were then maintained in an anesthetic plane with 1-2% isoflurane in oxygen and kept at a body temperature of 36°C with the use of a homeothermic blanket. Prior to any surgical procedure, mice were administered subcutaneous injections of sustained release buprenorphine (1mg/kg) for analgesia, dexamethasone (0.2mg/kg) for reduction of swelling, and bupivacaine (2mg/kg), for local anesthesia. Mice received a subcutaneous injection of an antibiotic, enrofloxacin (Baytril; 5mg/kg), for 3 days as part of their post-operative care.

Viral Injections.

Approximately 21 days prior to electrophysiological recordings or transcardial perfusions, we performed small (0.5mm in diameter) unilateral craniotomies using a micromotor drill (Foredom)–under aseptic conditions–over audTRN or MGB. Glass syringes–attached to a syringe pump (Pump 11 Elite, Harvard Apparatus)–were backfilled with modified viral vectors, placed over the brain region of interest, and used to inject virus at 60nL/min. Glass syringes were made using a micropipette puller (P-97, Sutter Instruments) from glass

capillaries (Harvard Apparatus, 30-0038) with tip openings ranging from 30µm-40µm in diameter. Following injections, syringes were left in place for 15-20min before retraction. Craniotomies were then covered with bone wax (Fine Science Tools) or a removable silicone plug (Kwik-Cast, World Precision Instruments). audTRN coordinates: -1.80mm posterior to bregma, ±2.25mm lateral to bregma, -2.90mm below the pial surface. MGB coordinates: -3.30mm posterior to bregma, ±2.00mm lateral to bregma, -2.90mm below the pial surface. Viral spread was confirmed post-mortem.

Viral Vectors.

For soma-targeted inactivation of PV or SST neurons of the audTRN we injected 400nL of AAV5_hSyn1-SIO-stGtACR1-FusionRed (full titer, Addgene 105678-AAV5). For anterograde tracing of PV or SST neurons of the audTRN and control experiments we injected 250nL or 400nL of AAV5-hSyn-DIO-mCherry (full titer, Addgene 50459-AAV5).

Fiber Optic Cannula & Headpost Implantation.

Following virus injections, fiber optic cannulas (Prizmatix: 3mm in length, 1.25mm in diameter, Ø200µm core, 0.66NA) were implanted above audTRN at a 20° angle, -1.80mm posterior to bregma, ±3.25mm lateral to bregma, and -2.50mm below the pial surface. A small craniotomy was made over the left frontal lobe and a ground pin was implanted. Craniotomies were sealed with Kwik-Cast (World Precision Instruments). The cannula, ground pin and a custom-made stainless-steel headpost (eMachine shop) were then secured with dental cement (C&B Metabond, Parkell) and dental acrylic (Lang Dental).

Tissue Processing.

After allowing time for proper viral expression or following electrophysiological recordings, mice were deeply anesthetized with a cocktail of ketamine and dexmedetomidine (see Animals) and transcardially perfused with 1X PBS followed by 4% paraformaldehyde (PFA) in PBS. Brains were extracted and post-fixed in 4% PFA overnight at 4°C. Following post-fixation, tissue was cryoprotected in 30% sucrose for at least 24hrs at 4°C until sectioning. Brain sections of 40µm-50µm in thickness were cut on a cryostat (Leica CM1860) and collected for immunohistochemistry or imaging of viral expression. For imaging of viral expression or probe location, 50µm-thick sections were mounted on gelatin-coated glass slides and coverslipped using ProLong Diamond Antifade

Mounting media with DAPI (Catalog # P36971, Invitrogen). For immunohistochemistry, 40μm-thick sections were collected in 12-well plates filled with 1X PBS (~5-10 sections per well). Slides were imaged using a fluorescent microscope (Leica DM6 B) or a confocal microscope (Zeiss LSM 800).

Immunohistochemistry.

Free-floating 40μm-thick brain sections were first washed in 1X PBS (3 x 10min washes). To increase membrane permeability, sections were microwaved for approximately 10 seconds and then incubated in a solution of 0.3% Triton X-100 in 1X PBS (hereinafter referred to as PBT) for 30 min at room temperature. The sections were then incubated in a blocking solution consisting of 5% normal goat serum in PBT (hereinafter referred to as PBTG) for 30min-1hr at room temperature. Following incubation with PBTG, sections were incubated in primary antibody solution which consisted of the following antibodies diluted in PBTG: (1) 1:500 mouse monoclonal anti-Parvalbumin (Swant, PV-235; RRID:AB_10000343), (2) 1:500 rabbit polyclonal anti-Somatostatin (Immunostar, 20067); RRID: AB_572264), and (3) 1:1000 rabbit polyclonal anti-Calretinin (Swant, Calretinin-7697; RRID:AB_2721226). Incubation in primary solution was done overnight-48hrs at 4°C on a shaker (Fisher Scientific); well plates were covered with parafilm and a plastic lid. Following the incubation period with primary antibody solution, sections were washed in PBT (3 x 10min washes). Sections were then incubated in secondary antibodies conjugated to fluorescent markers diluted in PBTG for 2hrs at room temperature; well plates were covered with aluminum foil to block light. Secondary antibodies used were: (1) Alexa Fluor Plus 488 Goat anti-Mouse IgG (H+L) (for PV stain; catalog # A32723, Invitrogen; RRID: AB_2633275), (2) Alexa Fluor Plus 488 Goat anti-Rat IgG (H+L) (for SST stain; Catalog # A48262, Invitrogen; RRID: AB_2896330), and (2) Alexa Fluor Plus 488 Goat anti-Rabbit IgG (H+L) (for Calretinin stain; Catalog # A32731, Invitrogen; RRID: AB_2633280). Sections were then incubated for 10min in a 1:40,000 dilution of DAPI stock solution in PBT (5mg/mL, Invitrogen; D1306). The sections were subsequently washed in 1X PBS (5 x 10min washes). Sections were then mounted on gelatin-coated glass slides, coverslipped using ProLong Diamond Antifade Mounting media (Catalog # P36970, Invitrogen) and left to curate on a flat surface at room temperature for at least 24hrs prior to imaging. Slides were then imaged using a fluorescent microscope (Leica DM6 B) or a confocal microscope (Zeiss LSM 800).

Acoustic Stimuli.

Stimuli were generated using custom MATLAB code and were sampled at 200kHz with a 32-bit resolution. Acoustic stimuli were delivered through a speaker (Multicomp by Newark, MCPCT-G5100-4139) positioned in the direction of the animals' ear contralateral to the recording site. To assess stimulus-locked auditory responses, we used a set of click trains made up of 5 broadband noise bursts at a rate of 1Hz. The noise bursts were 25ms long and presented at a rate of 10Hz for a total of 500ms. To assess frequency response functions in neuronal population, we generated a set of 19 pure tones of logarithmically spaced frequencies ranging between 3kHz and 80kHz at 70dB sound pressure level relative to 20μPa (SPL). Each tone was 50ms long with a 1ms cosine squared ramp, repeated 40 times with an inter-stimulus-interval of 300ms and presented in a pseudo-random order. 20 of those 40 tone repetitions were accompanied by a continuous laser pulse with a 1ms cosine squared ramp starting at tone onset and ending at tone offset (50ms long; for details on laser stimuli see Optogenetic Inactivation).

Optogenetic Inactivation and Calibration.

To inactivate populations of neurons, we injected a soma-targeted inhibitory opsin in the audTRN of PV- and SST-Cre mice (see Viral Injections and Viral Vectors). Laser-only recordings were achieved by delivering continuous (1ms cosine squared ramp) laser pulses of different durations (10ms, 25ms, 50ms, and 100ms) through an implanted fiber-optic cannula via a fiber-coupled blue LED (460nm, Prizmatix, Optogenetics-LED-Blue). Frequency tuning Laser_{On} trials were achieved by delivering a continuous 50ms pulse with a 1ms squared ramp.

To reduce variability in the effects of optogenetic manipulation across mice, we developed a procedure to calibrate the LED source prior to each recording session. Once the probe was in its final depth for recording, we presented alternating click trains (see Acoustic Stimuli) wherein each trial consisted of a click train without LED stimulation followed by a click train paired with LED stimulation with 20 different intensities (LED driving voltage ranged from 0 to 5V) while recording neural responses. This stimulus set was presented 10 times for each intensity value and neural responses were sorted offline using Kilosort2. To calculate if each unit was significantly sound responsive and discard noise clusters, we computed a Wilcoxon sign-rank test between the sound responses during the LED-off click trains and a baseline period of activity. Excluded units from further analysis are those whose P-values exceeded a Bonferroni-corrected α-level of $0.05/n_{\text{clusters}}$. We then calculated the

number of spikes during the LED_{off} click train trials (n_{OFF}) and during the LED_{on} click train trials (n_{ON}) and computed the percent change in the response (r_{PC}) for each light intensity:

$$r_{PC} = \frac{n_{ON} - n_{OFF}}{n_{OFF}} * 100$$

Using a logistic function, we fit the response function as a function of the LED voltage,

$$y = a + \frac{b}{1 + e^{-(x-c)d}}$$

where a determines the y-offset of the response, b determines the range of the response, c determines the x-offset, and d the gain of the response. With this fit equation, we found the voltage values that elicited a 100% increase (2-fold change) in neural spiking and used that value for the rest of the stimulus presented in each individual recording session. Some sessions did not show a 2-fold increase with LED manipulation; for these sessions we used maximum LED power for all stimuli.

Acute Electrophysiological Recordings.

All electrophysiological recordings were carried out in a double-walled acoustic-isolation booth (Industrial Acoustics). At least 21 days post-viral injection, animals were anesthetized (see Surgical Procedures) and a small craniotomy (1mm in diameter) was performed using a micromotor drill (Foredom) over MGB (for coordinates see Viral Injections). Mice were then clamped into a custom-base and allowed to recover from anesthesia for at least 30min. Following their recovery time, we vertically (0° on stereotaxic arm) lowered a 32-channel silicon probe (NeuroNexus: A1x32-Poly2-10mm-50s-177) to a depth of ~3.5mm from the pial surface using a motorized micromanipulator (Scientifica) attached to a stereotaxic arm (Kopf) at a rate of 1-2μm/s. While we lowered the probe, a train of brief broadband noise clicks were played (see Acoustic Stimuli), if we observed stimulus-locked responses, we determined the probe was in a sound-responsive area. The probe was coated in lipophilic far-red dye (Vybrant DiD, Invitrogen), to determine recording sites post-hoc (see Tissue Processing). Recordings that did not display stimulus-licked responses or were not determined to be in MGB, were not used in this analysis. Once the probe reached the target recording depth, it was left to settle in the brain for at least 30min prior to recording. Neural signals were amplified via an Intan headstage (RHD 32ch, Intan Technologies), recorded at a rate of 30kHz using an OpenEphys acquisition board and GUI[64] and digitized with an SPI cable. Signals were filtered between 500 and 6000Hz, offset corrected, and re-referenced to the median of all active channels. Recorded neural data was spike sorted using KiloSort2[65] and manually corrected using phy2. Upon

manual correction, units were classified as either single- or multi- units; if units exhibited a clear refractory period, they were labeled single units, otherwise they were classified as multi-units. Both single-units and multi-units were included in all analyses (for number of units used see Table 1). Approximately 3 recording sessions were achieved from each individual mouse at different recording sites.

Gray Value Analysis & Cell Counting.

Gray Value: We first delineated the MGB across the different ROI's. We then used Fiji's Plot Profile plug-in to output the gray values. Using a custom Python script we then calculated the mean gray values and S.E.M.

Cell Counting: We used the Cellpose[66] anatomical segmentation algorithm to outline cells in selected sections. We then manually confirmed the masks provided by Cellpose in Fiji using the cell counter plugin. A custom Python script was used to calculate the overlapping masks and percentages.

Neural Response Analysis.

Following manual spike sorting, units included in this analysis were selected based on their sound responsive profiles. To select sound-responsive units, we used the find_peaks function from SciPy's Python Library and set the minimum peak height to the mean of the baseline activity–calculated as the average firing rate 50ms prior to tone onset–+3 standard deviations of each unit. If units did not display peaks above this set criteria during the presentation of the tone in laser-Off conditions–calculated as the average firing rate during the first 25ms of tone presentation across all laser-off trials–they were labeled as non-sound responsive units and excluded from further analysis. Spontaneous firing rate was computed as the average firing rate during a time window of 50ms prior to tone onset ($FR_{Spontaneous}$) for both laser-Off and laser-On trials. Tone-evoked firing rate (FR_{Evoked}) was calculated as the average firing rate for the first 25ms (0-25ms) of the total tone duration (50ms). Late tone-evoked firing rate was calculated ($FR_{EvokedLate}$) was calculated as the average firing rate from 25ms to tone offset (25ms-50ms). Offset responses (FR_{Offset}) were calculated as the average firing rate during a 150ms time-window after tone offset. Laser only responses were calculated as the average firing rate during laser presentation. We calculated the difference in the response between laser-Off and laser-On conditions by subtracting the mean normalized firing rate during the first 25ms of tone presentation in the laser-Off trials and the mean normalized firing rate during the first 25ms of tone presentation in the laser-On trials. To calculate frequency response functions, we averaged the firing rate during early-tone presentation (0-25ms) for all the

trials of the individual 19 frequencies in both laser-Off and laser-On conditions and centered them to their best frequency. Best frequency is defined as the frequency that elicited the highest change in firing rate compared to baseline activity. Linear fits were calculated by using SciKit Learns Linear Regression Model (Python Library) on the mean firing rate of each cell for every repeat of each of the 19 frequencies. Using the outputs of this model, we extracted the slope and the y-intercepts of the fit for each unit's frequency response function.

Statistical Analysis.

We assessed normality of the data using a Shapiro-Wilk tests using Scipy's Stats Python Library. For paired data that violated the assumption of normality, p values were calculated using a Wilcoxon sign-rank tests using Scipy's Stats Python Library. For non-paired data that violated the assumption of normality, p values were calculated using a Wilcoxon rank-sum tests using Scipy's Stats Python Library. The standard error of the mean was used to calculate error bars (±SEM). Symbols: * indicates p values <0.05, ** indicates p values < 0.01, and *** indicates p values <0.001.

Modelling.

Model cells were Hodgkin-Huxley formalism solved by a second order Runge-Kutta ODE solver in MATLAB (ode23, Mathworks). Parameters were built upon those used previously [43,67,68], and included the following ionic currents and maximal conductances: fast transient Na+ (NaT) 60.5 mS/cm^2, K+ delayed rectifier (Kd) 60 mS/cm^2, K+ transient A (Kt) 5 mS/cm^2, slowly inactivating K+ (K2) 0.5 mS/cm^2, slow anomalous rectifier (AR) 0.025 mS/cm^2, and low threshold transient Ca2+ (CaT) 0.75 mS/cm^2 for PV/MGB cells and 0.375 mS/cm^2 for SST/HO cells. Reversal potentials were 50 mV for sodium, -100 mV for potassium, 125 mV for calcium, -40 mV for AR and -75 mV for leak. Capacitance was 1 μF/cm^2 with leak of 0.1 mS/cm^2. Chemical synapses were modelled as double exponential decay with rise and fall time kinetics of 5 ms and 35 ms respectively, with reversal potentials of 0 mV for excitatory and -100 mV for inhibitory synapses. Electrical synapses were modelled as static coupling conductance of 0.03 mS/cm^2 applied to the voltage difference between the coupled TRN cells, corresponding to a strong electrical coupling (~0.2 coupling coefficient). PSTH were obtained from spike time data histograms with a bin size of 1 ms and smoothed with a 31 ms Hanning window. We normalized each response to the maximum rate in the non-inactivated trial.

RESOURCE AVAILABILITY

Lead Contact

Further information and requests for resources and reagents should be directed to and will be fulfilled by the Lead Contact, Maria Geffen (mgeffen@pennmedicine.upenn.edu).

Data & Code availability

Source data has been deposited in Dryad: https://doi.org/10.5061/dryad.ht76hdrq5. Data analysis code is available on GitHub: https://github.com/geffenlab/Rolon_Martinez_2024. Code for the model is available at github: https://github.com/jhaaslab/TRN_MGB_celltypespecific.

Acknowledgements

The authors would like to thank the members of the Geffen laboratory and Yale Cohen for their discussions and helpful comments. This work was supported by the following grants from NIDCD: R01DC15527, R01DC014479, R03DC013660 to MNG, F31DC018473 to SRM, F31DC016524to CFA, from NINDS R01NS113241 to MNG and NIH R01 NS128713 to JSH.

REFERENCES

1. Blackwell, J.M., and Geffen, M.N. (2017). Progress and challenges for understanding the function of cortical microcircuits in auditory processing. Nat. Commun. *8*, 2165. https://doi.org/10.1038/s41467-017-01755-2.

2. Bartlett, E.L. (2013). The organization and physiology of the auditory thalamus and its role in processing acoustic features important for speech perception. Brain Lang. *126*, 29–48. https://doi.org/10.1016/j.bandl.2013.03.003.

3. He, J. (2003). Corticofugal modulation of the auditory thalamus. Exp. Brain Res. *153*, 579–590. https://doi.org/10.1007/s00221-003-1680-5.

4. Crabtree, J.W. (1998). Organization in the auditory sector of the cat's thalamic reticular nucleus. J. Comp. Neurol. *390*, 167–182. https://doi.org/10.1002/(sici)1096-9861(19980112)390:2<167::aid-cne1>3.0.co;2-%23.

5. Crabtree, J.W. (2018). Functional diversity of thalamic reticular subnetworks. Front. Syst. Neurosci. *12*, 41. https://doi.org/10.3389/FNSYS.2018.00041/BIBTEX.

6. Houser, C.R., Vaughn, J.E., Barber, R.P., and Roberts, E. (1980). GABA neurons are the major cell type of the nucleus reticularis thalami. Brain Res. *200*, 341–354. https://doi.org/10.1016/0006-8993(80)90925-7.

7. Pinault, D. (2004). The thalamic reticular nucleus: structure, function and concept. Brain Res. Rev. *46*, 1–31. https://doi.org/10.1016/J.BRAINRESREV.2004.04.008.

8. Aizenberg, M., Mwilambwe-Tshilobo, L., Briguglio, J.J., Natan, R.G., and Geffen, M.N. (2015). Bidirectional Regulation of Innate and Learned Behaviors That Rely on Frequency Discrimination by Cortical Inhibitory Neurons. PLoS Biol. *13*, 1–32. https://doi.org/10.1371/journal.pbio.1002308.

9. Clemente-Perez, A., Makinson, S.R., Higashikubo, B., Brovarney, S., Cho, F.S., Urry, A., Holden, S.S., Wimer, M., Dávid, C., Fenno, L.E., et al. (2017). Distinct Thalamic Reticular Cell Types Differentially Modulate Normal and Pathological Cortical Rhythms. Cell Rep. *19*, 2130–2142. https://doi.org/10.1016/j.celrep.2017.05.044.

10. Hamilton, L.S., Sohl-Dickstein, J., Huth, A.G., Carels, V.M., Deisseroth, K., and Bao, S. (2013). Optogenetic Activation of an Inhibitory Network Enhances Feedforward Functional Connectivity in Auditory Cortex. Neuron *80*, 1066–1076. https://doi.org/10.1016/j.neuron.2013.08.017.

11. Phillips, E.A., and Hasenstaub, A.R. (2016). Asymmetric effects of activating and inactivating cortical interneurons. eLife *5*. https://doi.org/10.7554/eLife.18383.

12. Phillips, E.A.K., Schreiner, C.E., and Hasenstaub, A.R. (2017). Cortical Interneurons Differentially Regulate the Effects of Acoustic Context. Cell Rep. *20*, 771–778. https://doi.org/10.1016/j.celrep.2017.07.001.

13. Seybold, B.A., Phillips, E.A.K., Schreiner, C.E., and Hasenstaub, A.R. (2015). Inhibitory Actions Unified by Network Integration. Neuron *87*, 1181–1192. https://doi.org/10.1016/J.NEURON.2015.09.013.

14. Ahrens, S., Jaramillo, S., Yu, K., Ghosh, S., Hwang, G.R., Paik, R., Lai, C., He, M., Huang, Z.J., and Li, B. (2015). ErbB4 regulation of a thalamic reticular nucleus circuit for sensory selection. Nat. Neurosci. *18*, 104–111. https://doi.org/10.1038/nn.3897.

15. Crick, F. (2006). Function of the thalamic reticular complex: the searchlight hypothesis. Proc. Natl. Acad. Sci. *81*, 4586–4590. https://doi.org/10.1073/pnas.81.14.4586.

16. Halassa, M.M., Chen, Z., Wimmer, R.D., Brunetti, P.M., Zhao, S., Zikopoulos, B., Wang, F., Brown, E.N., and Wilson, M.A. (2014). State-dependent architecture of thalamic reticular subnetworks. Cell *158*, 808–821. https://doi.org/10.1016/j.cell.2014.06.025.

17. Nakajima, M., Schmitt, L.I., and Halassa, M.M. (2019). Prefrontal Cortex Regulates Sensory Filtering through a Basal Ganglia-to-Thalamus Pathway. Neuron *103*, 445-458.e10. https://doi.org/10.1016/j.neuron.2019.05.026.

18. Schmitt, L.I., Wimmer, R.D., Nakajima, M., Happ, M., Mofakham, S., and Halassa, M.M. (2017). Thalamic amplification of cortical connectivity sustains attentional control. Nature *545*, 219–223. https://doi.org/10.1038/nature22073.

19. Wimmer, R.D., Schmitt, L.I., Davidson, T.J., Nakajima, M., Deisseroth, K., and Halassa, M.M. (2015). Thalamic control of sensory selection in divided attention. Nature *526*, 705–709. https://doi.org/10.1038/nature15398.

20. Guillery, R.W., and Sherman, S.M. (2002). Review Thalamic Relay Functions and Their Role in Corticocortical Communication: Generalizations from the Visual System.

21. Carroll, B.J., Sampathkumar, V., Kasthuri, N., and Sherman, S.M. (2022). Layer 5 of cortex innervates the thalamic reticular nucleus in mice. Proc. Natl. Acad. Sci. U. S. A. *119*. https://doi.org/10.1073/PNAS.2205209119.

22. Gentet, L.J., and Ulrich, D. (2004). Electrophysiological characterization of synaptic connections between layer VI cortical cells and neurons of the nucleus reticularis thalami in juvenile rats. Eur. J. Neurosci. *19*, 625–633. https://doi.org/10.1111/j.1460-9568.2004.03168.x.

23. Guo, W., Clause, A.R., Barth-Maron, A., and Polley, D.B. (2017). A Corticothalamic Circuit for Dynamic Switching between Feature Detection and Discrimination. Neuron *95*, 180-194.e5. https://doi.org/10.1016/j.neuron.2017.05.019.

24. Lam, Y.W., and Sherman, S.M. (2005). Mapping by laser photostimulation of connections between the thalamic reticular and ventral posterior lateral nuclei in the rat. J. Neurophysiol. *94*, 2472–2483. https://doi.org/10.1152/jn.00206.2005.

25. Lam, Y.W., and Sherman, S.M. (2011). Functional organization of the thalamic input to the thalamic reticular nucleus. J. Neurosci. *31*, 6791–6799. https://doi.org/10.1523/JNEUROSCI.3073-10.2011.

26. Natan, R.G., Briguglio, J.J., Mwilambwe-Tshilobo, L., Jones, S.I., Aizenberg, M., Goldberg, E.M., and Geffen, M.N. (2015). Complementary control of sensory adaptation by two types of cortical interneurons. eLife *4*. https://doi.org/10.7554/eLife.09868.

27. Natan, R.G., Rao, W., and Geffen, M.N. (2017). Cortical Interneurons Differentially Shape Frequency Tuning following Adaptation. Cell Rep. *21*, 878–890. https://doi.org/10.1016/j.celrep.2017.10.012.

28. Briguglio, J.J., Aizenberg, M., Balasubramanian, V., and Geffen, M.N. (2018). Cortical neural activity predicts sensory acuity under optogenetic manipulation. J. Neurosci. *38*, 2094–2105. https://doi.org/10.1523/JNEUROSCI.2457-17.2017.

29. Park, Y., and Geffen, M.N. (2019). A Unifying Mechanistic Model of the Auditory Cortex with Inhibitory Subtypes. bioRxiv, 626358. https://doi.org/10.1101/626358.

30. Moore, A.K., and Wehr, M. (2013). Parvalbumin-expressing inhibitory interneurons in auditory cortex are well-tuned for frequency. J. Neurosci. *33*, 13713–13723. https://doi.org/10.1523/JNEUROSCI.0663-13.2013.

31. Li, L.Y., Xiong, X.R., Ibrahim, L.A., Yuan, W., Tao, H.W., and Zhang, L.I. (2015). Differential Receptive Field Properties of Parvalbumin and Somatostatin Inhibitory Neurons in Mouse Auditory Cortex. Cereb. Cortex *25*, 1782–1791. https://doi.org/10.1093/cercor/bht417.

32. Ulanovsky, N., Las, L., and Nelken, I. (2003). Processing of low-probability sounds by cortical neurons. Nat. Neurosci. *6*, 391–398. https://doi.org/10.1038/nn1032.

33. Taaseh, N., Yaron, A., and Nelken, I. (2011). Stimulus-Specific Adaptation and Deviance Detection in the Rat Auditory Cortex. PLoS ONE *6*, e23369. https://doi.org/10.1371/journal.pone.0023369.

34. Fishman, Y.I., and Steinschneider, M. (2012). Searching for the mismatch negativity in primary auditory cortex of the awake monkey: Deviance detection or stimulus specific adaptation? J. Neurosci. *32*, 15747–15758. https://doi.org/10.1523/JNEUROSCI.2835-12.2012.

35. Farley, B.J., Quirk, M.C., Doherty, J.J., and Christian, E.P. (2010). Stimulus-Specific Adaptation in Auditory Cortex Is an NMDA-Independent Process Distinct from the Sensory Novelty Encoded by the Mismatch Negativity. J. Neurosci. *30*, 16475–16484. https://doi.org/10.1523/JNEUROSCI.2793-10.2010.

36. Polterovich, A., Jankowski, M.M., and Nelken, I. (2018). Deviance sensitivity in the auditory cortex of freely moving rats. PLoS ONE *13*, e0197678. https://doi.org/10.1371/journal.pone.0197678.

37. Martinez-Garcia, R.I., Voelcker, B., Zaltsman, J.B., Patrick, S.L., Stevens, T.R., Connors, B.W., Cruikshank, S.J., and Carney, N.D. (2020). Two dynamically distinct circuits drive inhibition in the sensory thalamus. Nature *583*. https://doi.org/10.1038/s41586-020-2512-5.

38. Lu, E., Llano, D.A., and Sherman, S.M. (2009). Different distributions of calbindin and calretinin immunostaining across the medial and dorsal divisions of the mouse medial geniculate body. Hear. Res. *257*, 16–23. https://doi.org/10.1016/J.HEARES.2009.07.009.

39. Mahn, M., Gibor, L., Patil, P., Cohen-Kashi Malina, K., Oring, S., Printz, Y., Levy, R., Lampl, I., and Yizhar, O. (2018). High-efficiency optogenetic silencing with soma-targeted anion-conducting channelrhodopsins. Nat. Commun. *9*, 4125. https://doi.org/10.1038/s41467-018-06511-8.

40. Ito, T., Bishop, D.C., and Oliver, D.L. (2011). Expression of glutamate and inhibitory amino acid vesicular transporters in the rodent auditory brainstem. J. Comp. Neurol. *519*, 316–340. https://doi.org/10.1002/CNE.22521.

41. Desai, N.V., and Varela, C. (2021). Distinct burst properties contribute to the functional diversity of thalamic nuclei. J. Comp. Neurol. *529*, 3726–3750. https://doi.org/10.1002/cne.25141.

42. Vaughn, M.J., Laswick, Z., Wang, H., and Haas, J.S. (2024). Functionally Distinct Circuits Are Linked by Heterocellular Electrical Synapses in the Thalamic Reticular Nucleus. eNeuro *11*. https://doi.org/10.1523/ENEURO.0269-23.2023.

43. Pham, T., and Haas, J.S. (2018). Electrical synapses between inhibitory neurons shape the responses of principal neurons to transient inputs in the thalamus: a modeling study. Sci. Rep. *8*, 7763. https://doi.org/10.1038/s41598-018-25956-x.

44. Pham, T., and Haas, J.S. (2019). Electrical synapses regulate both subthreshold integration and population activity of principal cells in response to transient inputs within canonical feedforward circuits. PLOS Comput. Biol. *15*, e1006440. https://doi.org/10.1371/journal.pcbi.1006440.

45. Hou, G., Smith, A.G., and Zhang, Z.-W. (2016). Lack of intrinsic GABAergic connections in the thalamic reticular nucleus of the mouse. J. Neurosci. *36*, 7246–7252.

46. Deleuze, C., and Huguenard, J.R. (2006). Distinct Electrical and Chemical Connectivity Maps in the Thalamic Reticular Nucleus: Potential Roles in Synchronization and Sensation. J. Neurosci. *26*, 8633–8645. https://doi.org/10.1523/JNEUROSCI.2333-06.2006.

47. Lam, Y.-W., Nelson, C.S., and Sherman, S.M. (2006). Mapping of the Functional Interconnections Between Thalamic Reticular Neurons Using Photostimulation. J. Neurophysiol. *96*, 2593–2600. https://doi.org/10.1152/jn.00555.2006.

48. Pinault, D., and Deschênes, M. (1998). Projection and innervation patterns of individual thalamic reticular axons in the thalamus of the adult rat: A three-dimensional, graphic, and morphometric analysis. J. Comp. Neurol. *391*, 180–203. https://doi.org/10.1002/(SICI)1096-9861(19980209)391:2<180::AID-CNE3>3.0.CO;2-Z.

49. Shosaku, A., Kayama, Y., Sumitomo, I., Sugitani, M., and Iwama, K. (1989). Analysis of recurrent inhibitory circuit in rat thalamus: Neurophysiology of the thalamic reticular nucleus. Prog. Neurobiol. *32*, 77–102. https://doi.org/10.1016/0301-0082(89)90011-7.

50. Crabtree, J.W., Collingridge, G.L., and Isaac, J.T.R. (1998). A new intrathalamic pathway linking modality-related nuclei in the dorsal thalamus. Nat. Neurosci. *1*, 389–394. https://doi.org/10.1038/1603.

51. Crabtree, J.W., and Isaac, J.T.R. (2002). New Intrathalamic Pathways Allowing Modality-Related and Cross-Modality Switching in the Dorsal Thalamus. J. Neurosci. *22*, 8754–8761. https://doi.org/10.1523/JNEUROSCI.22-19-08754.2002.

52. Oertel, W.H., Graybiel, A.M., Mugnaini, E., Elde, R.P., Schmechel, D.E., and Kopin, I.J. (1983). Coexistence of glutamic acid decarboxylase- and somatostatin-like immunoreactivity in neurons of the feline nucleus reticularis thalami. J. Neurosci. *3*, 1322–1332. https://doi.org/10.1523/JNEUROSCI.03-06-01322.1983.

53. Li, Y., Lopez-Huerta, V.G., Adiconis, X., Levandowski, K., Choi, S., Simmons, S.K., Arias-Garcia, M.A., Guo, B., Yao, A.Y., Blosser, T.R., et al. (2020). Distinct subnetworks of the thalamic reticular nucleus. Nature *583*. https://doi.org/10.1038/s41586-020-2504-5.

54. Lee, C.C., and Sherman, S.M. (2010). Drivers and Modulators in the Central Auditory Pathways. Front. Neurosci. *4*, 79. https://doi.org/10.3389/neuro.01.014.2010.

55. Winer, J.A. (2005). Decoding the auditory corticofugal systems. Hear. Res. *207*, 1–9. https://doi.org/10.1016/j.heares.2005.06.007.

56. Deschesˆnes, M., Madariaga-Domich, A., and Steriade, M. (1985). Dendrodendritic synapses in the cat reticularis thalami nucleus: a structural basis for thalamic spindle synchronization. Brain Res. *334*, 165–168. https://doi.org/10.1016/0006-8993(85)90580-3.

57. Yen, C.T., Conley, M., Hendry, S.H., and Jones, E.G. (1985). The morphology of physiologically identified GABAergic neurons in the somatic sensory part of the thalamic reticular nucleus in the cat. J. Neurosci. Off. J. Soc. Neurosci. *5*, 2254–2268. https://doi.org/10.1523/JNEUROSCI.05-08-02254.1985.

58. Asanuma, C., and Porter, L.L. (1990). Light and electron microscopic evidence for a GABAergic projection from the caudal basal forebrain to the thalamic reticular nucleus in rats. J. Comp. Neurol. *302*, 159–172. https://doi.org/10.1002/cne.903020112.

59. Herrera, C.G., Cadavieco, M.C., Jego, S., Ponomarenko, A., Korotkova, T., and Adamantidis, A. (2015). Hypothalamic feedforward inhibition of thalamocortical network controls arousal and consciousness. Nat. Neurosci. *19*, 290–298. https://doi.org/10.1038/nn.4209.

60. Paré, D., Hazrati, L.N., Parent, A., and Steriade, M. (1990). Substantia nigra pars reticulata projects to the reticular thalamic nucleus of the cat: a morphological and electrophysiological study. Brain Res. *535*, 139–146. https://doi.org/10.1016/0006-8993(90)91832-2.

61. Asanuma, C. (1989). Axonal arborizations of a magnocellular basal nucleus input and their relation to the neurons in the thalamic reticular nucleus of rats. Proc. Natl. Acad. Sci. *86*, 4746–4750. https://doi.org/10.1073/pnas.86.12.4746.

62. Belén Pardi, M., Vogenstahl, J., Dalmay, T., Spanò, T., Pu, D.L., Naumann, L.B., Kretschmer, F., Sprekeler, H., and Letzkus, J.J. (2020). A thalamocortical top-down circuit for associative memory. Science *370*, 844–848. https://doi.org/10.1126/SCIENCE.ABC2399/SUPPL_FILE/ABC2399_PARDI_SM.PDF.

63. Johnson, K.R., Tian, C., Gagnon, L.H., Jiang, H., Ding, D., and Salvi, R. (2017). Effects of Cdh23 single nucleotide substitutions on age-related hearing loss in C57BL/6 and 129S1/Sv mice and comparisons with congenic strains. Sci. Rep. *7*, 44450. https://doi.org/10.1038/srep44450.

64. Siegle, J.H., López, A.C., Patel, Y.A., Abramov, K., Ohayon, S., and Voigts, J. (2017). Open Ephys: an open-source, plugin-based platform for multichannel electrophysiology. J. Neural Eng. *14*, 045003. https://doi.org/10.1088/1741-2552/aa5eea.

65. Pachitariu, M., Sridhar, S., and Stringer, C. (2023). Solving the spike sorting problem with Kilosort. Preprint at bioRxiv, https://doi.org/10.1101/2023.01.07.523036 https://doi.org/10.1101/2023.01.07.523036.

66. Stringer, C., Wang, T., Michaelos, M., and Pachitariu, M. (2021). Cellpose: a generalist algorithm for cellular segmentation. Nat. Methods *18*, 100–106. https://doi.org/10.1038/s41592-020-01018-x.

67. Destexhe, A., Bal, T., McCormick, D.A., and Sejnowski, T.J. (1996). Ionic mechanisms underlying synchronized oscillations and propagating waves in a model of ferret thalamic slices. J. Neurophysiol. *76*, 2049–2070. https://doi.org/10.1152/jn.1996.76.3.2049.

68. Traub, R.D., Contreras, D., Cunningham, M.O., Murray, H., LeBeau, F.E.N., Roopun, A., Bibbig, A., Wilent, W.B., Higley, M.J., and Whittington, M.A. (2005). Single-Column Thalamocortical Network Model Exhibiting Gamma Oscillations, Sleep Spindles, and Epileptogenic Bursts. J. Neurophysiol. *93*, 2194–2232. https://doi.org/10.1152/jn.00983.2004.